11th World Congress on Computational Mechanics (WCCM XI)
5th European Conference on Computational Mechanics (ECCM V)
6th European Conference on Computational Fluid Dynamics (ECFD VI)
E. Oñate, J. Oliver and A. Huerta (Eds)

NUMERICAL TRANSITION PREDICTION IN A STRAIGHT TURBINE CASCADE

A. Petersen*

* Institute of Propulsion Technology
German Aerospace Center
Bunsenstraße 10, 37073 Göttingen, Germany
e-mail: anna.petersen@dlr.de, web page: www.DLR.de

Key words: straight turbine cascade, boundary layer transition, γ-Re$_\theta$ transition model

Abstract. This paper presents a variety of different numerical set-ups for the simulation of a straight turbine cascade flow. The DLR TRACE code was employed for the numerical investigations. Special emphasis is laid on the transition prediction applying the γ-Re$_\theta$ transition model. The γ-Re$_\theta$ transition model with different underlying turbulence models and turbulence model modifications are varied. The numerical investigations are compared to experimental data obtained at the Wind Tunnel for Straight Cascades at DLR, Göttingen. For comparison with the experimental data one exit Mach number at a low transonic region and two different incidence angles are investigated. For the measurement infrared imaging, Schlieren photography, pressure taps and hot-wire-anemometry are applied.

1 INTRODUCTION

The main tasks in improving aircraft turbines are to reduce the losses and to increase the loads. This paper presents experimental and numerical investigations of a straight turbine cascade with the main focus on transition prediction. The turbine blades are designed within the EC project TFAST (Transition location effect on shock wave boundary layer interaction) for increased loads. Additionally, the accelerated flow region upstream of the shock is designed for relaminarization of the boundary layer. The retained laminar boundary layer decreases the friction losses. A 3D-computation is performed but the investigation concentrates on 2D-effects at turbine mid-span [1]. Sidewall effects through secondary flow are neglected.

Experimental investigations are performed at the Wind Tunnel for Straight Cascades at the German Aerospace Center (DLR), Göttingen [2]. The Wind Tunnel operates according to the blow down principle and is supplied with ambient air. The inlet conditions are measured using a hot-wire-probe as well as a 3-hole-probe. Two different incidence

angles are investigated at an isentropic exit Mach number of Ma $\approx$ 0.9 and a chord Reynolds number of $R_{ec} \approx 1.1$ million. To determine the transition location infrared imaging, Schlieren technique, and pressure taps are applied. The 3D-flow through the turbine cascade is numerically investigated using the TRACE code. TRACE is developed at DLR, Institute of Propulsion Technology [3].

Pressure profiles and turbulence levels measured upstream of the cascade are used as inlet boundary condition for the numerical investigation. For transition prediction the γ-Re_θ transition model [4, 5] is used. Fully turbulent computations with the Wilcox k-ω model [6] and the Menter SST k-ω model [7] as underlying turbulence models are performed. In addition, various turbulence limiters and turbulence model modifications for rotational and streamline curvature effects are applied.

The numerical results are compared to the experimental findings. In the numerical investigation special emphasis is set on the influence of the applied numerical settings on the transition location.

2 NUMERICAL METHODS

2.1 Geometry

The stator cascade of a high-pressure turbine is investigated. The turbine blade is not twisted in spanwise direction and has no tip clearance. Fig. 1 shows the turbine blade and the computational grid. The pitch ratio to the axial chord is $\frac{t}{c_{ax}} \approx 2$. In both Y-directions are periodic boundaries.

2.2 Computational grid

The spatial discretization of the channel passage field is obtained by an OCGH multi-block structured grid topology (Fig. 1). For all computational cases the maximum wall distance (y+) is below 1. A grid-sensitivity-study at subsonic and supersonic exit Mach numbers shows no difference from finer meshes by more than 0.3 %. At the exit plane a comparison is done with respect to the flow angle, mass flow and pressure. Additionally the resulting blade force and the total pressure loss were regarded. The finer mesh consists of 8.8 and 15 million nodes. The comparison of a 1 million node mesh showed a deviation in the total pressure loss of approximately one percent. Therefore, the mesh consisting four million nodes is appropriate and is applied for this investigation. On this blade are 356 grid points.

2.3 Flow Solver Set-up

The calculations are performed with the DLR TRACE code [3]. For the steady computations a finite volume approach for the three dimensional Reynolds-averaged Navier-Stokes (RANS) equations is used. The convective fluxes are discretized by Roe's second-order-accurate upwind scheme [8]. The transition location is predicted by the application of the γ-Re_θ transition model [4, 5]. The γ-Re_θ model is implemented in TRACE with

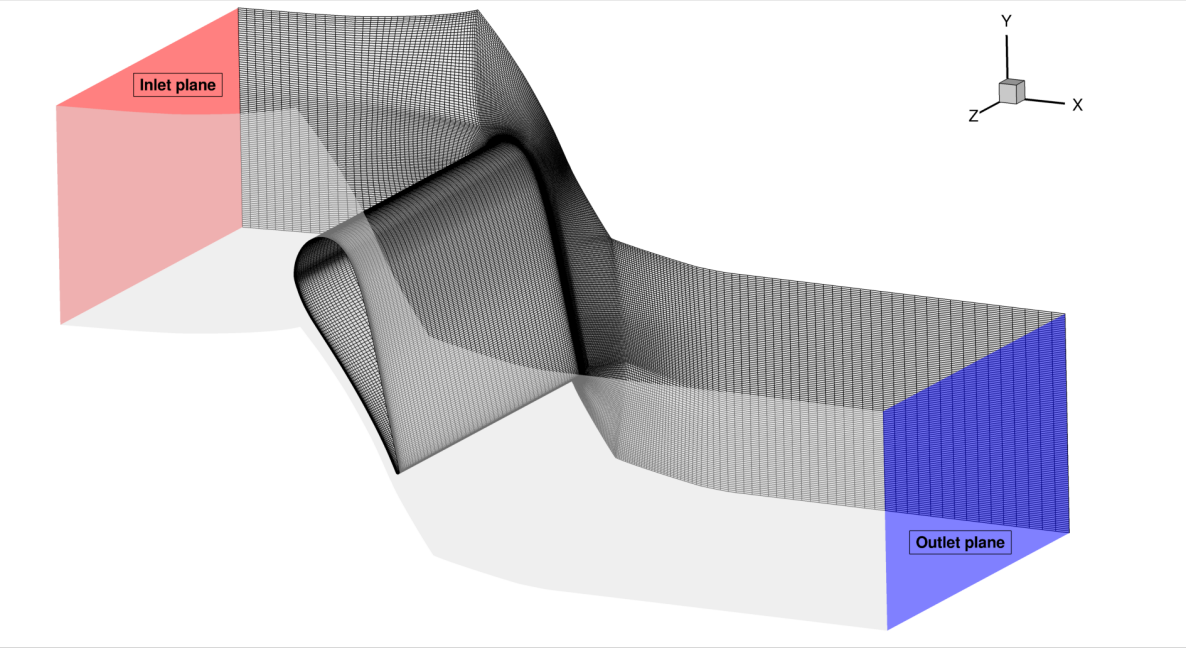

Figure 1: Discretization of the turbine stator geometry

the empirical correlations by Malan et al. [9, 10].

In Tab. 1 are listed different turbulence model settings. The underlying turbulence model will be varied between Wilcox k-ω model [6] and the Menter SST k-ω model [7]. The Kato-Launder modification and Schwarz limitation are compared [11]. In addition, various turbulence model modification for rotational and streamline curvature effects are tested [12], [13]. The applicable set-up cases for this configuration are listed in Tab. 1. The last column shows similar pressure distributions (Sim. p.) and refers to Fig. 2 in section 4.

2.4 Boundary Conditions

At the inlet plane (Fig. 1) measured wind tunnel data are deployed. With a hot-wire-anemometer were highly resolved velocity data taken. The turbulence intensity and the turbulence length scale are calculated from the measured data (section 3.2) and employed as numerical inlet conditions. The distance of inlet plane to the blade is approximately equal as the distance of hot-wire-probe and blade.

The inlet temperature and pressure is averaged for all test conditions. The inlet pressure is set to p = 99500 Pa and the inlet temperature to T = 293 K. The maximum temperature deviation from the average is ΔT = 2.85 K and the highest pressure aberration Δp = 567 Pa. The exit conditions were predetermined by an isentropic evaluation. The exit Mach number is set to Ma $\approx$ 0.9 and the flow incidence angles are $\alpha = 0°$ and $\alpha = 30°$.

Table 1: Variations of numerical settings

Set-up	Turbulence model	Stagnation point	Rotational effects	Sim. p.
1	Wilcox k-ω	Schwarz	Off	a
2	Wilcox k-ω	Schwarz	Bardina	a
3	Wilcox k-ω	Schwarz	StreamLine Curvature	a
4	Wilcox k-ω	Kato-Launder	Off	b
5	Wilcox k-ω	Kato-Launder	Bardina	b
6	Wilcox k-ω	Kato-Launder	StreamLine Curvature	a
7	Menter SST k-ω	Schwarz	Off	c
8	Menter SST k-ω	Schwarz	Bardina	c
9	Menter SST k-ω	Kato-Launder	Off	c
10	Menter SST k-ω	Kato-Launder	Bardina	c

3 EXPERIMENTAL METHODS

3.1 Test facility

The measurements were performed at the Wind Tunnel for Straight Cascades at the German Aerospace Center in Göttingen. The wind tunnel operates with the blow down principle and aspirates ambient air. The flow is contracted and introduced into the test section. The flow exits the test section through an adjustable diffusor and enters a 10,000 m^3 vacuum vessel [2].

The pressure and temperature of the inlet air are constant at ambient condition. Due to the fact that no drier is available only subsonic downstream Mach numbers can be investigated. The dew point is low enough and only high subsonic values are of interest. Within the present study the experimental results are not affected by condensation.

A detailed description of the installed probes and their accuracy as well as a description of the exit conditions by applying the equations of conservation of mass, momentum and energy are given in [2], [14] and [15].

3.2 Inlet measurements

For the inlet measurements a hot-wire-probe and a Cobra probe is deployed. The hot-wire-probe operates as a constant temperature anemometer. Previously to the measurement the velocity data are allocated by calibration. During the test the cascade was installed to induce the correct test conditions upstream of the cascade. The probe gauges at one fixed height in X- and Y-direction and various positions in Z-Direction (compare coordinate system in Fig. 1).

The turbulence length scale (L) is calculated by the autocorrelation of the velocity fluctuation. The Taylor-hypothesis allows the calculation of the turbulence length scale [16]:

$$L = \int_{t=\infty}^{t_0} \frac{\overline{u'(t) \cdot u'(t+\tau)}}{\overline{u'^2}} d\tau \cdot \bar{u}. \tag{1}$$

The turbulence intensity (Tu) is defined as the root mean square of the velocity fluctuation over the mean velocity:

$$Tu = \frac{\sqrt{\overline{u'^2}}}{\bar{u}}. \tag{2}$$

At the midsection the turbulence intensity is Tu ≈ 0.4 % and the turbulence length scale is L $\approx 3 \cdot 10^{-4}$ m. A Cobra probe was taken for the measurement of the inlet pressure [17].

3.3 Measurement Techniques

There is a conventional arrangement of the Schlieren visualization as described in [2]. For surface pressure distribution measurements the midspan of a blade was equipped with 20 pressure taps.

A black plastic blade is deployed for the infrared measurement. The thermal conductivity coefficient has an amount of 0.24. Bräunling [18] elaborates the advantage of the plastic material for infrared measurements. Furthermore does he say that the infrared thermography takes advantage of the change of local stresses which results in changes in the local heat transfer. While the heat transfer in laminar- and turbulent boundary layers and within a separation bubble is not the same, the temperature on the blade surface which is carried over the boundary layer differs depending on the boundary layer state. For this measurement a Nikon S270 Camera was employed.

4 RESULTS

All computational results are convergence well. Set-up 9 and 10 showed problems in the convergence.

The pressure distribution was measured at the incidence angle $\alpha = 0°$. The pressure distribution is shown from the throat regime to the leading of the suction side in Fig. 2. The measured data are compared to the CFD results. Similar numerical curves are presented by one of them. The outline of the similar curves can be found in the last column of Tab. 1. Qualitatively there is a good agreement. However, no numerical curve fits the experimental data in close agreement.

Fig. 3 shows three Schlieren pictures at the incidence angle $\alpha = 0°$ and random points of time. The red line in the picture indicates roughly the transition location. In every picture the red line is adjusted on the same picture height. In streamwise direction on the blade the first shock is an oblique shock. It is subjected to strong fluctuations as can be seen in Fig. 3. The second shock is identified as a normal shock where the flow

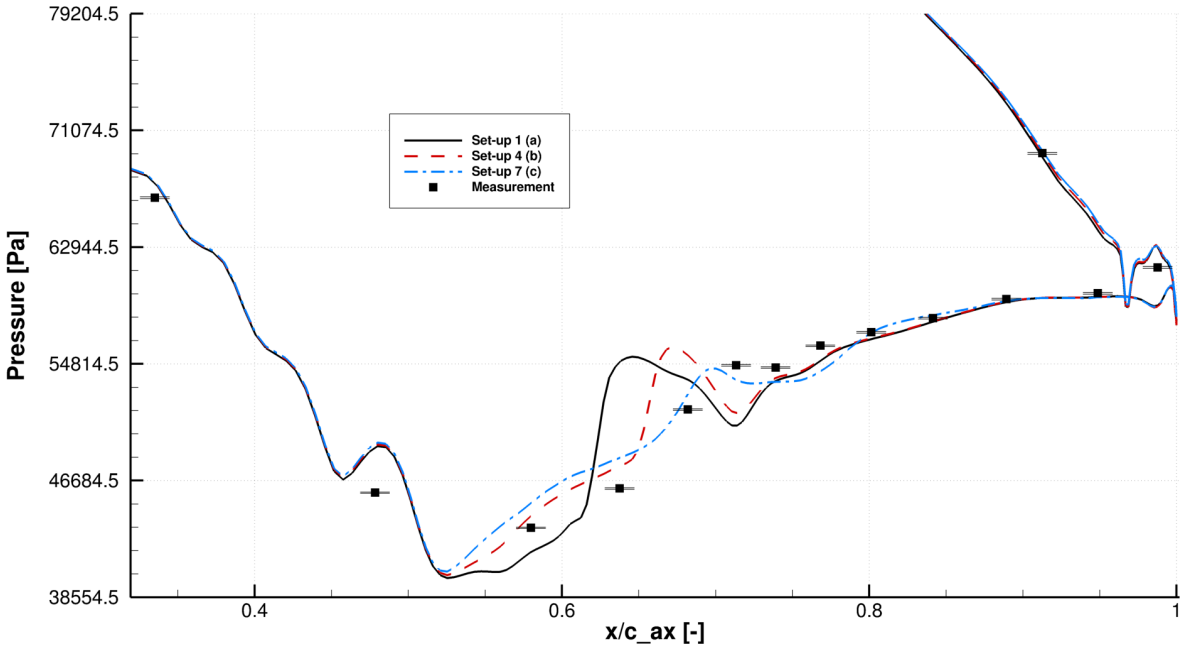

Figure 2: Detail view of the pressure distribution at incidence angle $\alpha = 0°$

velocity becomes subsonic [19]. The transition occurs at the normal shock. The transition position is not steady as it moves slightly (see Fig. 3).

Fig. 4 shows three Schlieren pictures at the incidence angle $\alpha = 30°$ and random points of time. There is also upstream an oblique and downstream a normal shock. At this incidence angle the transition location is slightly unsteady, too.

The average of the transition location is taken from the Schlieren pictures. The difference of the average is approximately 2 %. For the two incidence angles are slightly different positions determined and marked with a vertical aligned bold solid line in Fig. 5 (a) and (b). In these figures the scaled wall shear stresses of the suction side over the relative blade X-coordinate (Fig. 1) of the CFD calculations are shown. The wall shear stress is scaled on its maximum value for a better survey of the data.

The black squares are indicating the position on the abscissa for each set-up where the intermittency reaches the value of 0.5. The intermittency is a local variable and the presented results are averaged within the boundary layer. The averaged data are projected in normal direction on the blade's surface [20].

Fig. 5 (a) shows that the transition location of set-up 7, 9 and 10 lays downstream of the experimental transition location and close to the trailing edge. This is in contrast with all other set-ups where a better transition prediction is achieved. In Fig. 5 (b) only slight differences are revealed. The slight shift upstream of the measured transition location with respect to the transition location at the incidence angle $\alpha = 0°$ was not detected through the numerical simulations. Set-up 7, 9 and 10 are still predicting the

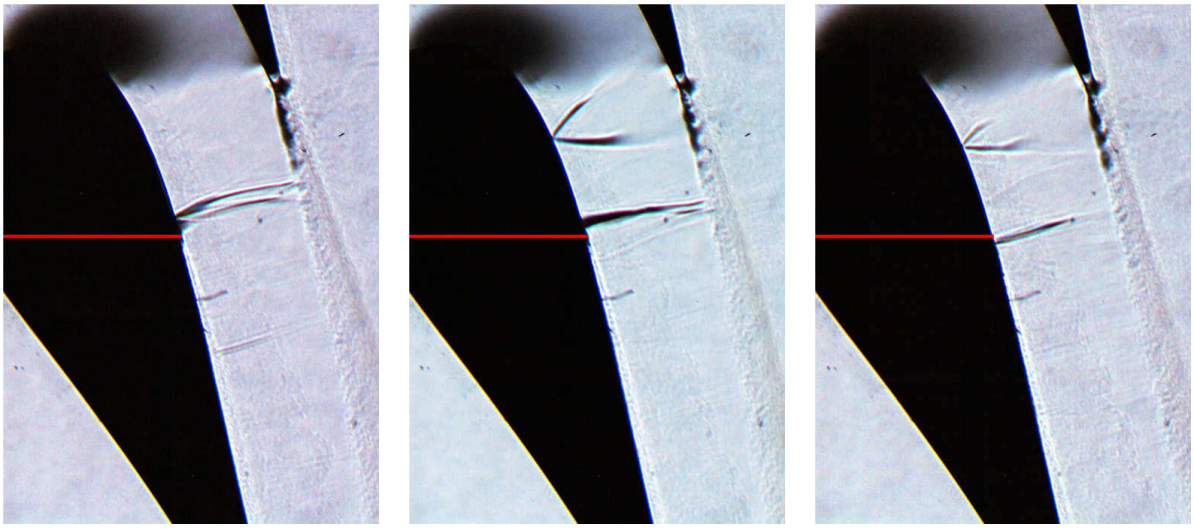

(a) (b) (c)

Figure 3: Schlieren pictures at incidence angle $\alpha = 0°$ (knife edge across to the blade chord)

transition location downstream of the measurement. In Fig. 5 (a) and (b) it seems that the turbulence model has an influence on the prediction of the transition location. To reflect upon the influence of the transition model a comparison of the recovery temperature on the suction side is made in Fig. 6 using set-up 1 and 7. The only variance of this set-ups concerns the underlying turbulence model (Tab. 1) and the convergence for both cases is acceptable. However, the transition location is very different.

Fig. 6 shows the recovery temperature on the suction side of the blade. The infrared image (a) shows a difference of a measurement with and without flow. The yellow circle in the middle of the picture is a reflection which has to be neglected. The numerical results (b) and (c) show the temperature difference with respect to the adiabatic wall temperature. The adiabatic wall temperature is equal to the inlet temperature. On the upper side in each picture in Fig. 6 is the leading edge of the blade and the flow goes down to the trailing edge. The upper thick black line marks the upper edge of the infrared image (a) and the lower thin line marks the measured transition position which is taken from the Schlieren photography.

In the experiment is no adiabatic wall (section 3.3) like in the computation. Therefore, one would not find an exact agreement. A good conformity is shown of the infrared result and set-up 1 anyway. On the upper side the temperature difference is around ΔT = -7 K to -8 K and starts to warm up until the trailing edge reaches a temperature difference of ΔT = -5 K. In contrast set-up 7 shows other temperatures. Downstream of the thick black line are the temperatures differences above ΔT = -3.5 K and it starts to cool down. In Fig. 6 (b) lays the measured transition location in a region which warms up in contrast to Fig. 6 (c) where the temperature is still above ΔT = -3.5 K. Hence, in Fig. 6 (b) can be

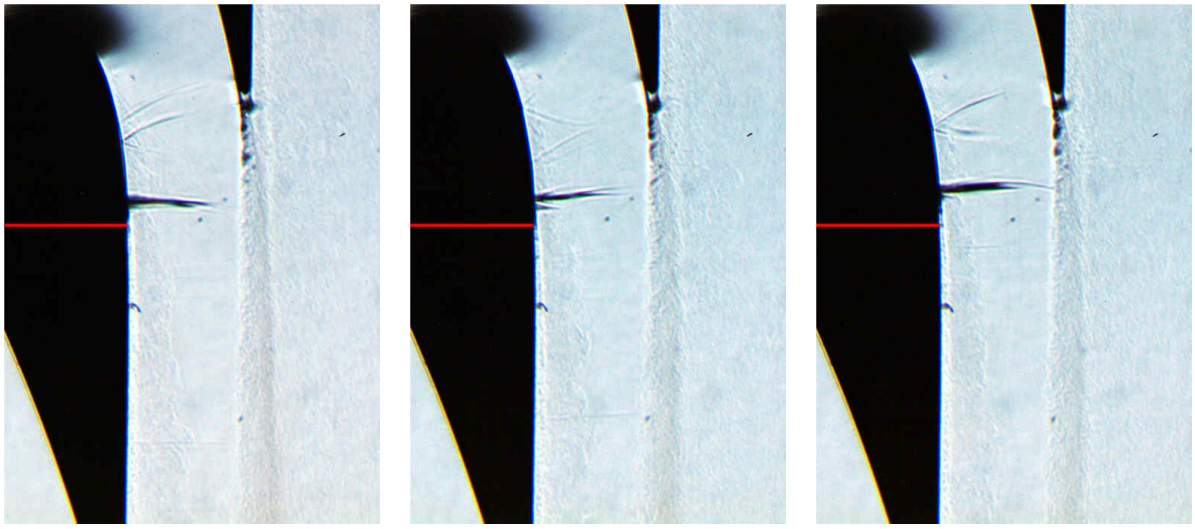

(a) (b) (c)

Figure 4: Schlieren pictures at incidence angle $\alpha = 30°$ (knife edge across to the blade chord)

found a better conformity to the measurement concerning the location of the transition than in Fig. 6 (c).

5 CONCLUSIONS

In this paper the main objective is to compare the transition location of experimental results to numerical simulations. A variety of different CFD set-ups is used and the γ-Re_θ transition model applied for transition prediction in all computations. Experimental techniques like Schlieren photography, infrared technique, pressure taps and hot-wire-anemometry are applied.

It is found that the employed turbulence model has a pronounced influence on the transition location. The same numerical set-up with the Wilcox k-ω model and the Menter SST k-ω model gives different results for the transition location. The Wilcox k-ω model agrees better in comparison to the measured data. The transition location is reliable predicted with the Wilcox k-ω model.

In a future investigation unsteady numerical simulations will be done. These results will be compared to unsteady measurements. The influence of the shock-wave-boundary-layer interaction requires more sophisticated measurement techniques. A higher transonic Mach number is a more complicated flow condition. For higher transonic Mach numbers dry air has to be used in the experimental set-up. Furthermore, an investigation of cooling orifices would be of high interest as they are used in the real engine.

ACKNOWLEDGEMENT

This is research was supported by 7 EU framework project and was carried out within research project of acronym TFAST (Transition Location Effect on Shock Wave Boundary Layer Interaction).

REFERENCES

[1] Denton, J. D. Loss Mechanisms in Turbomachines. *Journal of Turbomachinery* (1993) **115**:621–656.

[2] Kost, F. and Giess, P.-A. Experimental Turbine Research at DLR Goettingen. *Journal of the Gas Turbine Society of Japan* (2004) **32(6)**:485–493.

[3] Yang, H.; Kersken, H.-P. and Nuernberger, D. Toward Excellence in Turbomachinery Computational Fluid Dynamics: A Hybrid Structured-Unstructured Reynolds-Averaged Navier-Stokes Solver. *Journal of Turbomachinery* (2005) **128**:390–402.

[4] Menter, F. R.; Langtry, R. B.; Likki, S. R.; Suzen, Y. B.; Huang, P. G. and Volker, S. A. Correlation-Based Transition Model Using Local Variables: Part I — Model Formulation. *ASME Conf. Proc.* (2004) **2004**:57–67.

[5] Langtry, R. B.; Menter, F. R.; Likki, S. R.; Suzen, Y. B.; Huang, P. G. and Volker, S. A. Correlation-Based Transition Model Using Local Variables: Part II — Test Cases and Industrial Applications. *ASME Conf. Proc.* (2004) **2004**:69–79.

[6] Wilcox, D. A. Simulation of Transition with a Two-Equation Turbulence Model. *AIAA Journal* (1994) **32**:247–255.

[7] Menter, F. R. Two-equation eddy-viscosity turbulence models for engineering applications. *AIAA Journal* (1994) **32**:1598–1605.

[8] Roe P. Approximate Riemann solvers, parameter vectors, and difference schemes. *Journal of Computational Physics* (1981) **43**:357–372.

[9] Marciniak V.; Kügeler, E. and Franke, M. Predicting Transition on low-pressure Turbine Profiles. *In V European Conference on Computational Fluid Dynamics ECCOMAS CFD* (2010).

[10] Malan, P.; Suluksna, K. and Juntasaro, E. Calibrating the Gamma-Re_ theta Transition Model for Commercial CFD. *AIAA* (2009) **47**:1142.

[11] Röber, T.; Kožulović, D.; Kügeler, E. and Nürnberger, D. Appropriate Turbulence Modelling for Turbomachinery Flows using a Two-Equation Turbulence Model. *Notes on Numerical Fluid Mechanics and Multidisciplinary Design (NNFM)* (2006) **92**:446–454.

[12] Kožulović, D. and Röber, T. Modelling the Streamline Curvature Effects in Turbomachinery Flows. *In Proceedings of ASME Turbo Expo* (2006) No. GT2006-90265.

[13] Bardina, J.; Ferziger, J. H. and Rogallo, R. S. Effect of rotation on isotropic turbulence: computation and modelling. *Journal of Fluid Mechanics, Cambridge Journals Online* (1985) **154**:321–336.

[14] Rehder, H.-J. Investigation of Trailing Edge Cooling Concepts in a High Pressure Turbine Cascade–Aerodynamic Experiments and Loss Analysis. *Journal of Turbomachinery* (2012) **134**:051029–051029.

[15] Amecke, J. and Safarik, P. Data Reduction of Wake Flow Measurements with Injection of an other Gas. *DLR-Forschungsbericht* (1995) **1995**:95–32.

[16] Rotta, J. C. *Turbulente Strömungen Eine Einführung in die Theorie und ihre Anwendung*. Universitätsverlag Göttingen, Reprint of first Edition, (2010).

[17] Kost F. THE BEHAVIOUR OF PROBES IN TRANSONIC FLOW FIELDS OF TURBOMACHINERY. *8th European Conference on Turbomachinery - Fluid Dynamics and Thermodynamics.* (2009).

[18] Bräunling, W.; Quast, A. and Dietrichs, H.-J. Detection of Separation Bubbles by Infrared Images in Transonic Turbine Cascades. *Journal of Turbomachinery* (1988) **110**:504–511.

[19] Babinsky, H.; Harvey, J. K. *Shock Wave-Boundary-Layer Interactions*. Cambridge University Press, Vol. I., (2011).

[20] Marciniak, V.; Longhitano, M. and Kügeler E. Assessment of Transition Modeling for the Design of Controlled Diffusion Airfoil Compressor Cascades. *Proceedings of ASME Turbo Expo 2013* (2013).

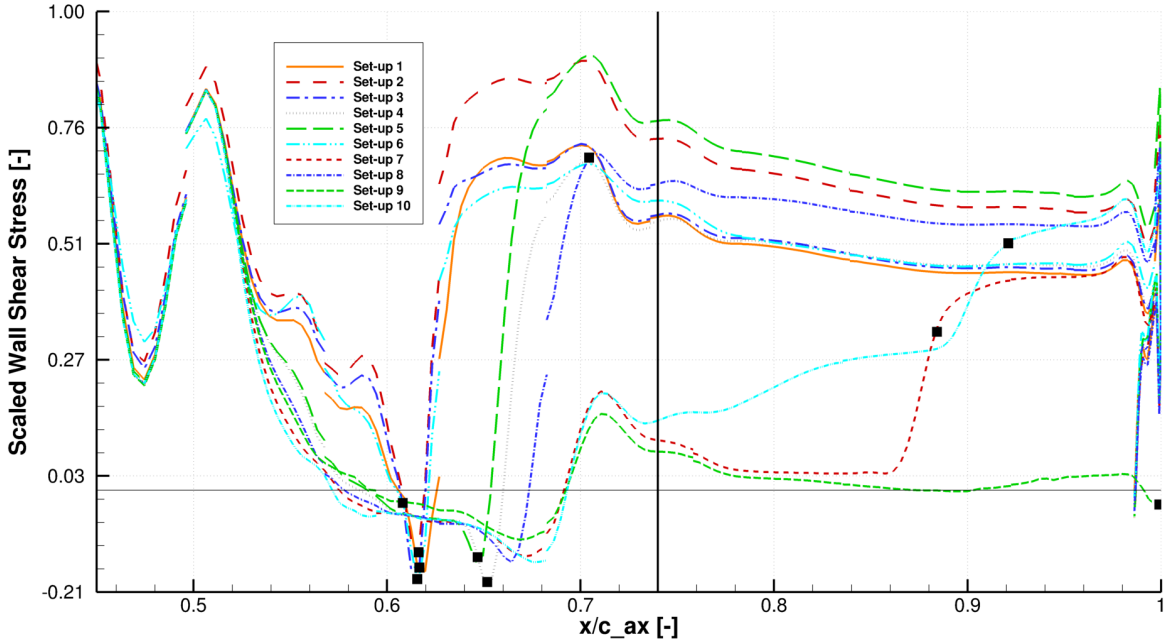

(a) Incidence angle $\alpha = 0°$

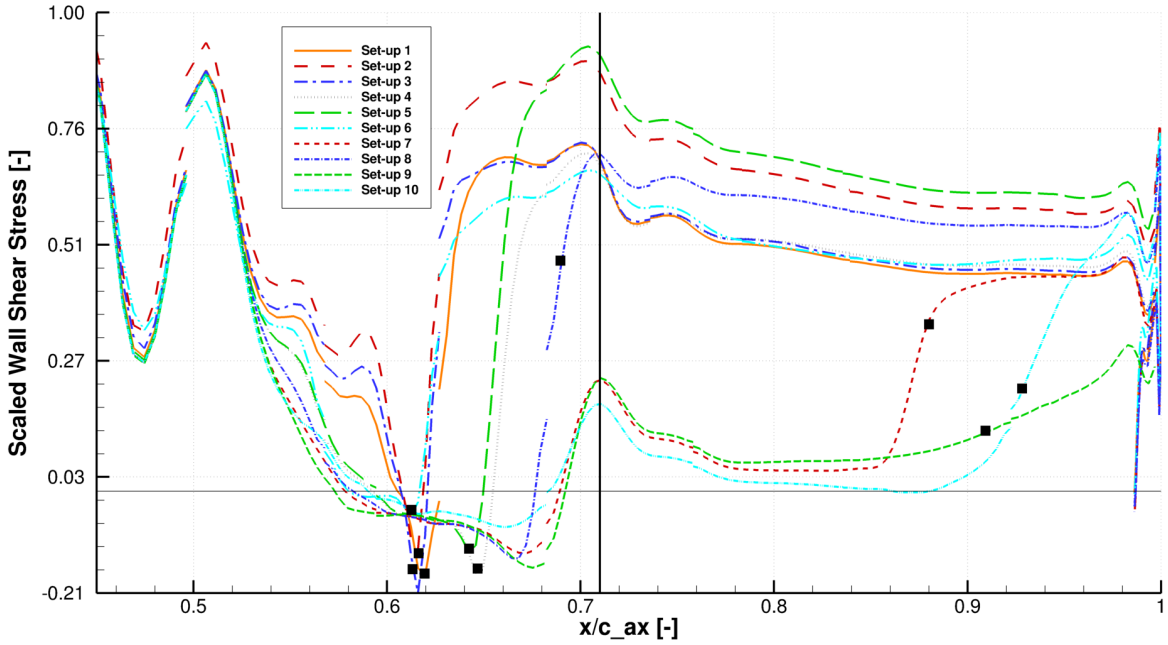

(b) Incidence angle $\alpha = 30°$

Figure 5: Comparison of intermittency and shear stress of the suction side

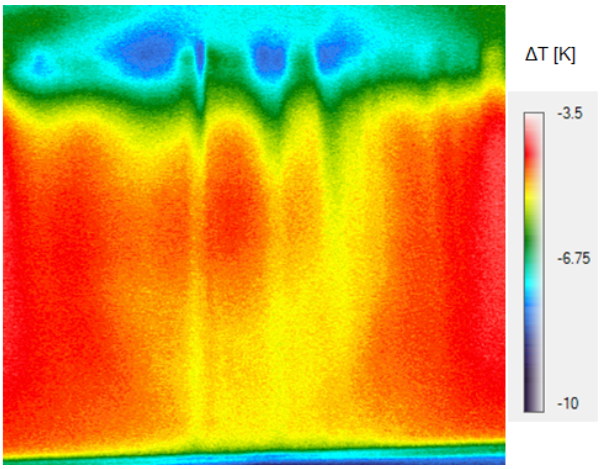

(a) Measurement

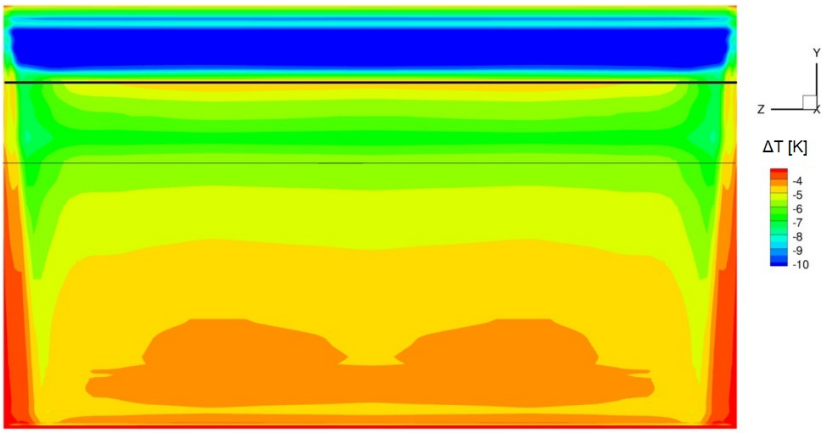

(b) Set-up 1

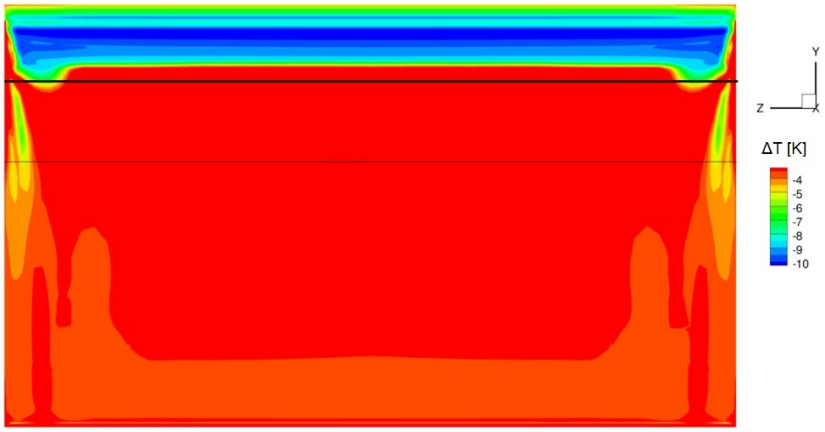

(c) Set-up 7

Figure 6: Recovery Temperature of suction side at incidence angle $\alpha = 0°$